

Highlights

Strong form mesh-free hp -adaptive solution of linear elasticity problem

Mitja Jančič, Gregor Kosec

- hp -adaptive strong form mesh-free method operating on scattered nodes.
- IMplicit-EXplicit (IMEX) error indicator.
- Mesh-free hp -adaptive solution of two- and three-dimensional linear elasticity problems.

Strong form mesh-free hp -adaptive solution of linear elasticity problem

Mitja Jančič^{a,b}, Gregor Kosec^{a,*}

^a*Institute Jožef Stefan, Parallel and distributed systems laboratory, Jamova Cesta 39, 1000 Ljubljana, Slovenia*

^b*Institute Jožef Stefan International Postgraduate School, Jamova Cesta 39, 1000 Ljubljana, Slovenia*

Abstract

We present an algorithm for hp -adaptive collocation-based mesh-free numerical analysis of partial differential equations. Our solution procedure follows a well-established iterative solve–estimate–mark–refine paradigm. The solve phase relies on the Radial Basis Function-generated Finite Differences (RBF-FD) using point clouds generated by advancing front node positioning algorithm that supports variable node density. In the estimate phase, we introduce an Implicit-Explicit (IMEX) error indicator, which assumes that the error relates to the difference between the implicitly obtained solution (from the solve phase) and a local explicit re-evaluation of the PDE at hand using a higher order approximation. Based on the IMEX error indicator, the modified Texas Three Step marking strategy is used to mark the computational nodes for h -, p - or hp -(de-)refinement. Finally, in the refine phase, nodes are repositioned and the order of the method is locally redefined using the variable order of the augmenting monomials according to the instructions from the mark phase.

The performance of the introduced hp -adaptive method is first investigated on a two-dimensional Peak problem and further applied to two- and three-dimensional contact problems. We show that the proposed IMEX error indicator adequately captures the global behaviour of the error in all cases considered and that the proposed hp -adaptive solution procedure significantly outperforms the non-adaptive approach. The proposed hp -adaptive method stands for another important step towards a fully autonomous numerical method capable of solving complex problems in realistic geometries without the user intervention.

Keywords: RBF-FD, hp -adaptivity, mesh-free, linear elasticity, error indicator

1. Introduction

Many natural and technological phenomena are modelled through Partial Differential Equations (PDEs), which can rarely be solved analytically – either because of geometric complexity or because of the complexity of the model at hand. Instead, realistic simulations are performed numerically. There are well-developed numerical methods that can be implemented in a more or less effective numerical solution procedure and executed on modern computers to perform virtual experiments or simulate the evolution of various natural or technological phenomena. Nonetheless, despite the immense computing power at our disposal, which allows us to solve ever more complex problems numerically, the development of efficient numerical approaches is still crucial. Relying solely on brute force computing often leads to unnecessarily long computations – not to mention wasted energy.

Most numerical solutions are obtained using mesh-based methods such as the Finite Volume Method (FVM), the Finite Difference Method (FDM), the Boundary Element Method (BEM) or the Finite Element Method (FEM). Modern numerical analysis is dominated by FEM [1] as it offers a mature and versatile solution approach that includes all types of adaptive solution procedures [2] and well understood error indicators [3]. Despite the widespread acceptance of FEM, the meshing of realistic 3D domains, a crucial part of FEM analysis where nodes are structured into polyhedrons covering the entire domain of interest, is still a problem that often requires user assistance or development of domain-specific algorithms [4].

*Corresponding author

Email address: gregor.kosec@ijs.si (Gregor Kosec)

In response to the tedious meshing of realistic 3D domains, required by FEM, and the geometric limitations of FDM and FVM, a new class of mesh-free methods [5] emerged in the 1970s. Mesh-free methods do not require a topological relationship between computational nodes and can therefore operate on scattered nodes, which greatly simplifies the discretisation of the domain [6], regardless of its dimensionality or shape [7, 8, 9]. Just recently, they have also been promoted to Computer Aided Design (CAD) geometry aware numerical analysis [10]. Moreover, the formulation of mesh-free methods is extremely convenient for implementing h -refinement [11], considering different approximations of partial differential operators in terms of the shape and size of the *stencil* [12, 13] and the local approximation order [14]. However, they methods tend to be more computationally intensive as they require larger stencils for stable computations [15, 14] and have limited preprocessing capabilities [16]. This may make them less attractive from a computational point of view, but the ability to work with scattered nodes and easily control the approximation order makes them good candidates for many applications in science and industry [17, 18].

Adaptive solution procedures are essential in problems where the accuracy of the numerical solution varies spatially and are currently subject of intensive studies. Two conceptually different adaptive approaches have been proposed, namely p -adaptivity or h -, ε -adaptivity. In p -adaptivity, the accuracy of the numerical solution is varied by changing the order of approximation, while in h - and ε -adaptivity, the resolution of the spatial discretisation is adjusted for the same purpose. In the h -adaptive approach, nodes are added or removed from the domain as needed, while in the ε -adaptive approach the total number of nodes remains constant – the nodes are only repositioned with respect to the desired accuracy. Ultimately, h - and p -adaptivities can be combined to form the so-called hp -adaptivity [19, 20, 21], where the accuracy of the solution is controlled with the order of the method and the resolution of the spatial discretisation.

Since the regions where higher accuracy is required are often not known *a priori*, and to eliminate the need for human intervention in the solution procedure, a measure of the quality of the numerical solution, commonly called a posterior error indicator, is a necessary additional step in an adaptive solution procedure [4]. The most famous error indicator, commonly referred to as the ZZ-type error indicator, was introduced in 1987 by Zienkiewicz and Zhu [22] in the context of FEM and it is still an active research topic [23]. The ZZ-type error indicator assumes that the error of the numerical solution is related to the difference between the numerical solution and a locally recovered solution. The ZZ-type error indicator has also been employed in the context of mesh-free solutions of elasticity problems using the mesh-free Finite Volume Method [24] in both weak and strong form using the Finite Point Method [25]. Furthermore, it also served as an inspiration in the context of Radial Basis Function-Generated Finite Difference (RBF-FD) solution to Laplace equation [26]. Moreover, a residual-based class of error indicators [27] has been demonstrated in the elasticity problems using a Discrete Least Squares mesh-free method [28]. Nevertheless, the most intuitive error indicators are based on the physical interpretation of the solution, usually evaluating the first derivative of the field under consideration [12] or calculating the variance of the field values within the support domain [11].

The advent of hp -adaptive numerical analysis began with FEM in the 1980s [29]. In hp -FEM, for example, one has the option of splitting an element into a set of smaller elements or increasing its approximation order. This decision is often considered to be the main difficulty in implementing the hp -adaptive solution procedure and was already studied by Babuška [29] in 1986. Since then, various decision-making strategies, commonly referred to as marking strategies, have been proposed [2, 30]. The early works use a simple Texas Three Step algorithm, originally proposed in the context of BEM [31], where the refinement is based on the maximum value of the error indicator. The first true hp -strategy was presented by Ainsworth [32] in 1997, since then many others have been proposed [2, 30]. In general, p - in FEM is more efficient when the solution is smooth. Based on this observation, most authors nowadays use the local Sobolev regularity estimate to choose between the h - and the p -refinement [33, 34, 35] for a given finite element. Moreover, in [36] local boundary values are solved, while the authors of [37, 38] use minimisation of the global interpolation error methods.

For mesh-free methods, h -adaptivity comes naturally with the ability to work with scattered nodes, and as such has been thoroughly studied in the context of several mesh-free methods [39, 40, 41]. Only recently, the popular Radial Basis Function-generated Finite Differences (RBF-FD) [42] have been used in the h -adaptive solution of elliptic problems [26, 43] and contact problems [11]. Researchers have also reported the combination of h - and ε -adaptivity, which form a so-called hr -adaptive solution procedure [44]. The p -adaptive method, on the other hand, is still quite unexplored in the mesh-free community. However, the authors of [45] approach the p -adaptive RBF-FD method in solving Poisson's equation with the idea of varying the order of the augmenting monomials to maintain the global order of convergence over the domain regardless of the potential variations in the spatial discretisation distance. It should

also be noted that some authors reported p -adaptive methods by locally increasing the number of shape functions, changing the interpolation basis functions, or simply increasing the stencil size [46, 47, 48]. These approaches are all to some extent p -adaptive, but not in their true essence. The authors of [49] have introduced a p -refinement with spatially variable local approximation order and come closest to a true p -adaptive solution procedure on scattered nodes. However, this work lacks an automated marking and refinement strategy for the local approximation order, e.g. based on an error indicator. The automated marking and refinement strategies were used with the weak form h - p adaptive clouds [50], where the authors use grid-like h -enrichment to improve the local field description.

In this paper, we present our attempt to implement the hp -adaptive strong form mesh-free solution procedure using the mesh-free RBF-FD approximation on scattered nodes. Our solution procedure follows a well-established paradigm based on an iterative loop. To estimate the accuracy of the numerical solution, we employ original IMEX error indicator. The marking strategy used in this work is based on the Texas Three Step algorithm [35], where the basic idea is to estimate the smoothness or analyticity of the numerical solution. Our refinement strategy is based on the recommendations of [11], where the authors were able to obtain satisfactory results using a purely h -adaptive solution procedure for elasticity problems. Although the chosen refinement and marking strategies are not optimal [37], the obtained results clearly outperform the non-adaptive approach.

2. hp -adaptive solution procedure

In the present work, we focus on the implementation of mesh-free hp -adaptive refinement, which combines the advantages of h - and p -refinement procedures. The proposed hp -adaptive solution procedure follows the well-established paradigm based on an iterative loop, where each iteration step consists of four modules:

1. **Solve** – A numerical solution \hat{u} is obtained.
2. **Estimate** – An error indication of the obtained numerical solution.
3. **Mark** – Marking of nodes for refinement/de-refinement.
4. **Refine** – Refinement/de-refinement of the spatial discretisation and local approximation order of the numerical method.

The workings of each module are further explained in the following subsections, while a full hp -adaptive solution procedure algorithm is given in Algorithm 1. For clarity, Figure 1 also graphically sketches the ultimate goal of a single refinement iteration.

Algorithm 1 hp -adaptive solution procedure

Input: The problem, computational domain Ω , initial nodal density function $h : \Omega \rightarrow \mathbb{R}$, initial approximation order distribution $m : \Omega \rightarrow \mathbb{N}$, the maximal number of iterations I_{\max} and adaptivity parameters $\alpha_{h,p}, \beta_{h,p}, \lambda_{h,p}, \vartheta_{h,p}$.

Output: The hp -refined numerical solution of the problem.

```

1: function ADAPTIVE_SOLVE(problem,  $\Omega, h, m, I_{\max}, \alpha_{h,p}, \beta_{h,p}, \lambda_{h,p}, \vartheta_{h,p}$ )
2:   for  $i \leftarrow 0$  to  $I_{\max}$  do
3:      $\Omega^* \leftarrow \text{DISCRETISE}(\Omega, h)$                                  $\triangleright$  Discretises domain using nodal density function  $h$ .
4:     solution  $\leftarrow \text{SOLVE}(\text{problem}, \Omega^*, m)$                  $\triangleright$  Obtains a numerical solution to the problem.
5:     indicator  $\leftarrow \text{IMEX}(\text{problem}, \text{solution}, \Omega^*, m)$          $\triangleright$  Error indicator computation.
6:     if STOPPING_CRITERIA then
7:       return solution
8:     end if
9:      $h, m \leftarrow \text{ADAPT}(\text{indicator}, h, m, \Omega^*, \alpha_{h,p}, \beta_{h,p}, \lambda_{h,p}, \vartheta_{h,p})$      $\triangleright$  Refine the nodes and approximation orders.
10:   end for
11:   return solution
12: end function

```

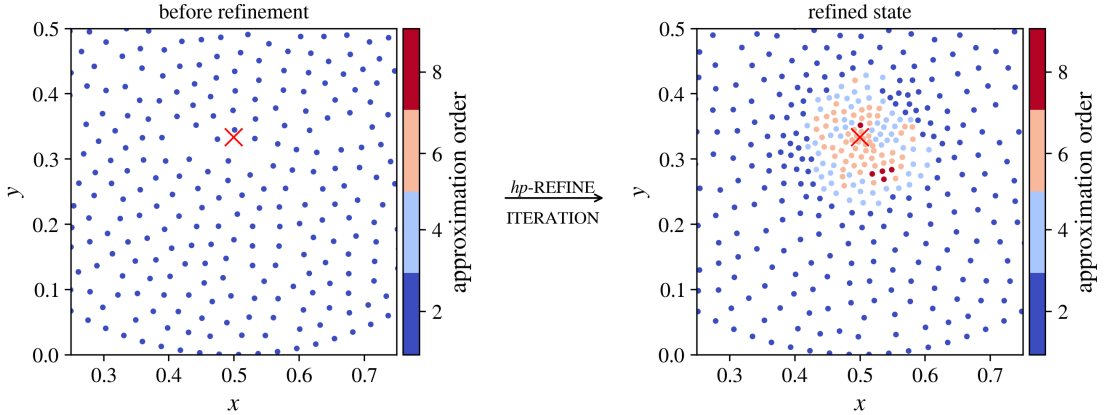


Figure 1: A sketch of a single hp -refinement iteration for a two-dimensional problem. Note that the exponentially strong source (marked with red cross) is set at $\bar{p} = (\frac{1}{2}, \frac{1}{3})$. The refined state has been obtained by employing h - and p -refinement strategies, thus the number of nodes and the local approximation orders in the neighbourhood of the strong source have been modified. Closed form solution has been used to indicate the error in the estimate module.

2.1. The SOLVE module

First, a numerical solution \hat{u} to the governing problem must be obtained. In general, the numerical treatment of a system of PDEs is done in several steps. First, the domain is discretised by positioning the nodes, then the linear differential operators in each computational node are approximated, and finally the system of PDEs is discretised and assembled into a sparse linear system. To obtain a numerical solution \hat{u} , the sparse system is solved.

Domain discretisation. While traditional mesh-based methods discretise the domain by building a mesh, mesh-free methods simplify this step to the positioning of nodes, as no information about internodal connectivity is required. With the mathematical formulation of the mesh-free methods being dimension-independent, we accordingly choose a dimension-independent algorithm for node generation based on Poisson disc sampling [51]. Conveniently, the algorithm also supports spatially variable nodal densities required by the h -adaptive refinement methods. An example of a variable node density discretisation can be found in Figure 2.

Interested readers are further referred to the original paper [51] for more details on the node generation algorithm, its stand-alone C++ implementation in the *Medusa library* [52], and follow-up research focusing on its parallel implementation [53] and parametric surface discretisations [54].

Approximation of linear differential operators. Having discretised the domain, we proceed to the approximation of linear differential operators. In this step, a linear differential operator \mathcal{L} is approximated over a set of neighbouring nodes, commonly referred to as *stencil nodes*.

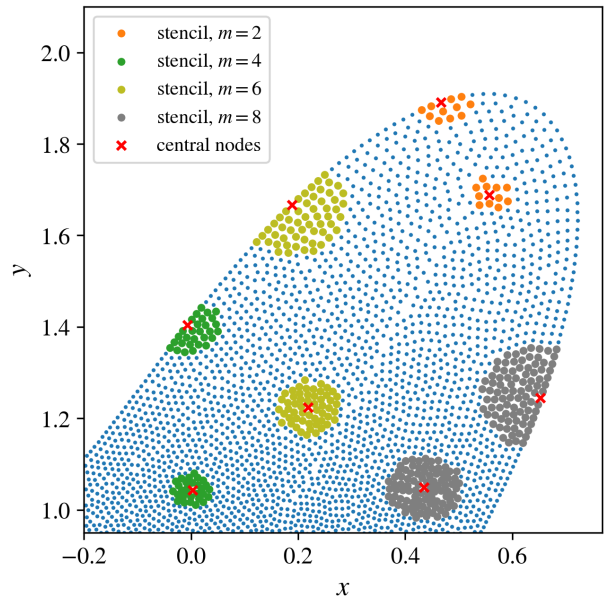


Figure 2: An example of domain discretisation with scattered nodes and variable node density. Example stencils are also shown for different approximation orders m on the domain boundary and its interior.

To derive the approximation, we assume a central point $\underline{x}_c \in \Omega$ and its stencil nodes $\{\underline{x}_i\}_{i=1}^n = \mathcal{N}$ for stencil size n . A linear differential operator in \underline{x}_c is then approximated over its stencil with the following expression

$$(\mathcal{L}u)(\underline{x}_c) \approx \sum_{i=1}^n w_i u(\underline{x}_i), \quad (1)$$

for an arbitrary function u and yet to be determined weights w which are computed by enforcing the equality of approximation (1) for a chosen set of basis functions.

In this work, we use Radial Basis Functions (RBFs) augmented with monomials. To eliminate the dependency on a shape parameter, we choose Polyharmonic Splines (PHS) [15] defined as

$$f(r) = \begin{cases} r^k, & k \text{ odd} \\ r^k \log r, & k \text{ even} \end{cases}, \quad (2)$$

for Euclidian distance r . The chosen approximation basis effectively results in what is commonly called the RBF-FD approximation method [42].

Furthermore, it is necessary that the stencil nodes form a so-called polynomial unisolvant set [55]. In this work, we follow the recommendations of Bayona [15] and define the stencil size as twice the number of augmenting monomials, i.e.

$$n = 2 \binom{m+d}{m} \quad (3)$$

for monomial order m and domain dimensionality d . This, in practice, results in large enough stencil sizes to satisfy the requirement, so that no special treatment was needed to assure unisolvency. While special stencil selection strategies showed promising results [12], a common choice for selecting a set of stencil nodes \mathcal{N} is to simply select the nearest n nodes. The latter approach was also used in this work. Figure 2 shows example stencils for different approximation orders m on domain boundary and its interior.

It is important to note that the augmenting monomials allow us to directly control the order of the local approximation method. The approximation order corresponds to the highest augmenting monomial order m in the approximation basis. However, the greater the approximation order the greater the computational complexity due to larger stencil sizes [14]. Nevertheless, the ability to control the local order of the approximation method sets the foundation for the p -adaptive refinement.

To conclude the solve module, the PDEs of the governing problem are discretised and assembled into a sparse system. The solution of the assembled system stands for the numerical solution \widehat{u} .

2.2. The ESTIMATE module (Implicit-Explicit error indicator)

In the estimation step, critical areas with high error of the numerical solution are identified. Identifying such areas is not a trivial task. In rare cases where a closed form solution to the governing problem exists, we can directly determine the accuracy of the numerical solution. Therefore, other objective metrics, commonly referred to as *error indicators*, are needed to indicate areas with high error of the numerical solution.

IMplicit-EXplicit (IMEX) error indicator. In this work we will use an error indicator based on the Implicit-Explicit [56] evaluation of the considered field. IMEX makes use of the implicitly obtained numerical solution and explicit operators (approximated by a higher order basis) to reconstruct the right-hand side of the governing problem. To explain the basic idea of IMEX, let us define a PDE of type:

$$\mathcal{L}u = f_{RHS}, \quad (4)$$

where \mathcal{L} is a differential operator applied to the scalar field u and f_{RHS} is a scalar function. To obtain an error indicator field η , the problem (4) is first solved implicitly by using a lower order approximation \mathcal{L}^{im} of operators \mathcal{L} , obtaining the solution u^{im} . The explicit high order operators \mathcal{L}^{ex} are then used over the implicitly computed field u^{im} to reconstruct the right-hand side of the problem (4) obtaining f_{RHS}^{ex} in the process. The error indication is then calculated as $\eta = |f_{RHS} - f_{RHS}^{ex}|$. The calculation steps of the IMEX error indicator are also shown in Algorithm 2.

Algorithm 2 IMEX error indicator

Input: The problem, domain Ω , differential operators \mathcal{L} , low-order approximation basis ξ , high order approximation basis ζ .

Output: Error indicator field η .

```

1: function INDICATE_ERROR(problem,  $\Omega$ ,  $\mathcal{L}$ ,  $\xi$ ,  $\zeta$ )
2:    $\mathcal{L}^{im} \leftarrow \text{APPROXIMATE}(\Omega, \xi)$                                  $\triangleright$  Obtain low-order approximation of differential operators  $\mathcal{L}$ .
3:    $u^{im}, f_{RHS} \leftarrow \text{SOLVE}(\text{problem}, \Omega, \mathcal{L}^{im})$            $\triangleright$  Obtain a numerical solution to the problem.
4:    $\mathcal{L}^{ex} \leftarrow \text{APPROXIMATE}(\Omega, \zeta)$                                  $\triangleright$  Obtain high order approximation of differential operators  $\mathcal{L}$ .
5:    $f_{RHS}^{ex} \leftarrow \text{EVALUATE}(\text{problem}, \Omega, \mathcal{L}^{ex}, u^{im})$            $\triangleright$  Explicit re-evaluation.
6:    $\eta \leftarrow \text{COMPUTE}(f_{RHS}, f_{RHS}^{ex})$                                  $\triangleright$  Obtain error indicator field.
7:   return  $\eta$ 
8: end function

```

The assumption that the deviation of the explicit high order evaluation $\mathcal{L}^{ex}u^{im}$ from the exact f_{RHS} corresponds to the error of the solution u^{im} is similar to the reasoning behind the ZZ-type indicators, where the deviation of the recovered high order solution from the computed solution characterises the error. As long as the error in u^{im} is high, the explicit re-evaluation will not correctly solve the equation (4). However, as the error in u^{im} decreases, the difference between f_{RHS} and f_{RHS}^{ex} will also decrease, assuming that the error is dominated by the inaccuracy of u_{im} and not by the differential operator approximation.

2.3. The MARK module

After the error indicator η has been obtained for each computational point in domain Ω , a marking strategy is applied. The main goal of this module is to mark the nodes with too high or too low values of the error indicator in order to achieve a uniformly distributed accuracy of the numerical solution and to reduce the computational cost – by avoiding fine local field descriptions and high order approximations where this is not required. Moreover, the marking strategy not only decides whether or not (de-)refinement should take place at a particular computational node, but also defines the type of refinement procedure if there are several to choose from. Here we use a modified Texas Three Step marking strategy [31, 35], originally restricted to refinement (no de-refinement) with the h - and p -refinement types. This chosen strategy was also considered in one of the recent papers by Eibner [35], who showed that, although extremely simple to understand and implement, it can provide results good enough to demonstrate the advantages of hp -adaptive solution procedures.

In each iteration of adaptive procedure, the marking strategy starts by checking the error indicator values η_i for all computational nodes in the domain. If η_i is greater than $\alpha\eta_{max}$ for maximum indicator value η_{max} and a free model parameter $\alpha \in (0, 1)$, the node is marked for refinement. If η_i is less than $\beta\eta_{max}$ for a free model parameter $\beta \in (0, 1) \wedge \beta \leq \alpha$, the node is marked for de-refinement. Otherwise, the node remains unmarked, which means that no refinement or de-refinement should take place. The marking strategy can be summarised with a single equation

$$\begin{cases} \eta_i > \alpha\eta_{max}, & \text{refine} \\ \beta\eta_{max} \leq \eta_i \leq \alpha\eta_{max}, & \text{do nothing} \\ \eta_i < \beta\eta_{max}, & \text{de-refine} \end{cases} \quad (5)$$

In the context of mesh-based methods, it has already been observed, that this strategy, although easy to implement, is far from optimal in terms of achieving good convergence rates. Our studies have shown that a slight modification to the originally proposed strategy can significantly improve the performance of an hp -adaptive solution procedure in the context of mesh-free methods, but at the cost of a higher number of free parameters – which also makes it more difficult to understand. Nevertheless, the strategy is modified by introducing parameters $\{\alpha_h, \beta_h\}$ and $\{\alpha_p, \beta_p\}$ for separate treatment of h - and p -refinements, respectively (see Figure 3 for clarification). Note that the proposed modified marking strategy can mark a particular node for h -, p - or hp -(de-)refinement if required, otherwise the computational node is left unchanged.

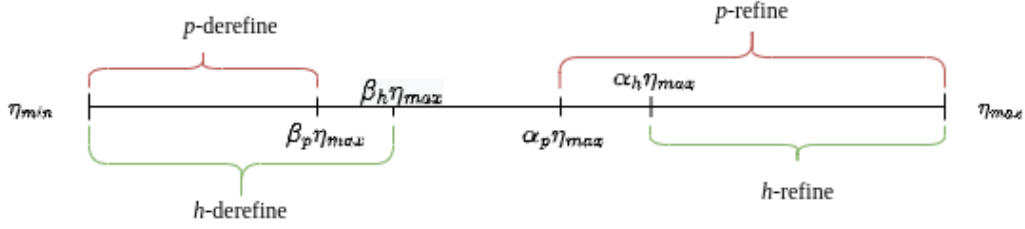


Figure 3: A visual representation of h - and p -(de)refinement marking strategy.

2.4. The REFINE module

After obtaining the list of nodes marked for modification, the refinement module is initialised. In this module, the local field description and local approximation order are left unchanged for the unmarked nodes, while the remaining nodes are further processed to determine other refinement-type-specific details – such as the amount of the (de-)refinement. Our h -refinement strategy is inspired by the recent h -adaptive mesh-free solution of elasticity problem [11], where the following h -refinement rule was introduced

$$h_i^{new}(\underline{p}) = \frac{h_i^{old}}{\frac{\eta_i - \alpha \eta_{max}}{\eta_{max} - \alpha \eta_{max}} (\lambda - 1) + 1} \quad (6)$$

for the dimensionless parameter $\lambda \in [1, \infty)$ allowing us to control the aggressiveness of the refinement – the larger the value, the greater the change in nodal density, as shown in Figure 4 on the left. This refinement rule also conveniently refines the areas with higher error indicator values more than those closer to the upper refinement threshold $\alpha_h \eta_{max}$. Similarly, a de-refinement rule is proposed

$$h_i^{new}(\underline{p}) = \frac{h_i^{old}}{\frac{\beta \eta_{max} - \eta_i}{\beta \eta_{max} - \eta_{min}} \left(\frac{1}{\vartheta} - 1 \right) + 1}, \quad (7)$$

where parameter $\vartheta \in [1, \infty)$ allows us to control the aggressiveness of de-refinement.

The same refinement (6) and de-refinement (7) rules are applied to control the order of local approximation (p -refinement), except that this time the value is rounded to the nearest integer, as shown in Figure 4 on the right. Similarly, and for the same reasons as for the marking strategy (see Section 2.3), we consider a separate treatment of h - and p -adaptive procedures by introducing (de-)refinement aggressiveness parameters $\{\lambda_h, \vartheta_h\}$ and $\{\lambda_p, \vartheta_p\}$ for h - and p -refinement types respectively.

2.5. Finalization step

Before the 4 modules can be iteratively repeated, the domain is re-discretised taking into account the newly computed local internodal distances $h_i^{new}(\underline{p})$ and the local approximation orders $m_i^{new}(\underline{p})$. However, both are only known in the computational nodes, while global functions $\widehat{h}^{new}(\underline{p})$ and $\widehat{m}^{new}(\underline{p})$ over our entire domain space Ω are required. Sheppard's inverse distance weighting interpolation using closest 30 and 3 is employed to obtain global functions $\widehat{h}^{new}(\underline{p})$ and $\widehat{m}^{new}(\underline{p})$, respectively.

Figure 5 schematically demonstrates 3 examples of hp -refinements. For demonstration purposes, the refinement parameters for h - and p -adaptivity are the same, i.e. $\{\alpha, \beta, \lambda, \vartheta\} = \{\alpha_h, \beta_h, \lambda_h, \vartheta_h\} = \{\alpha_p, \beta_p, \lambda_p, \vartheta_p\}$. Additionally, the de-refinement aggressiveness ϑ and the lower threshold β are kept constant, so that effectively only the upper limit of refinement α and the refinement aggressiveness λ are altered. We observe that the effect of the refinement parameters is somewhat intuitive. The greater the aggressiveness λ , the better the local field description and the greater the number of nodes with high approximation order. A similar effect is observed when manipulating the upper refinement threshold α , except that the effect comes at a smoother manner. Note also that all refined states were able to increase the accuracy of the numerical solution from the initial state.

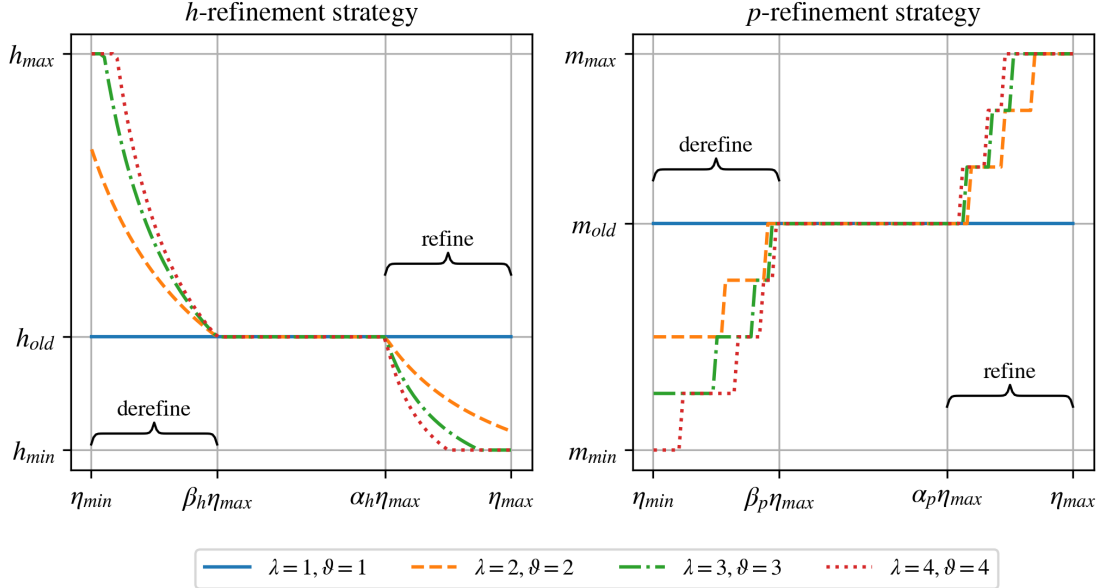


Figure 4: A visual representation of the (de-)refinement strategies for different values of refinement aggressiveness λ and de-refinement aggressiveness ϑ . Notice that both refinement types also have lower and upper limits.

2.6. Note on marking and refinement strategies

With the chosen marking and refinement strategies, a separate treatment of h - and p -refinement types turned out to be a necessary complication for a better overall performance of the solution procedure. Nevertheless, we have tried to simplify the solution procedure as much as possible. In the process, important observations have been made – some of which we believe should be highlighted. This section therefore opens a discussion on important remarks related to the proposed marking and refinement modules.

The error indicators. Since the h - and p -refinements are conceptually different, our first attempt was to employ two different error indicators – one for each type of refinement. We employed the previously proposed variance of field values [11] for marking the h -refinement and the approximation order based IMEX for the p -refinement. Unfortunately, no notable advantages of such solution procedure has been observed and was therefore discarded due to the increased implementation complexity. However, other combinations that might show more promising results should be considered in future work.

Free parameters. In the proposed solution procedure, each adaptivity type comes with 4 free parameters that need to be defined, i.e. $\{\alpha_{h,p}, \beta_{h,p}, \lambda_{h,p}, \vartheta_{h,p}\}$. This gives a total of 8 free parameters that can be fine-tuned to a particular problem. While we have tried to avoid any kind of fine-tuning, we have nevertheless observed that these parameters can have a crucial impact on the overall performance of the hp -adaptive solution procedure in terms of (i) the achieved accuracy of the numerical solution, (ii) the spatial variability of the error of the numerical solution, (iii) the computational complexity, and (iv) the stability of the solution procedure. We observed that if the refinement aggressiveness λ_h is too high, the number of nodes can either diverge into unreasonably large domain discretisations or ultimately violate the quasi-uniform internodal spacing requirement, making the solution procedure unstable. Furthermore, a large number of nodes combined with high approximation orders can lead to unreasonably high computational complexity in a matter of few iterations. However, when refinement aggressiveness λ_h and λ_p is set too low, the number of required iterations can increase to such an extent that the entire solution procedure becomes ineffective. On top of that, the lower and upper threshold multipliers α and β also play a crucial role. If α is too low, almost the entire domain is refined, which does not necessarily lead to an optimal node or approximation order distributions. Moreover,

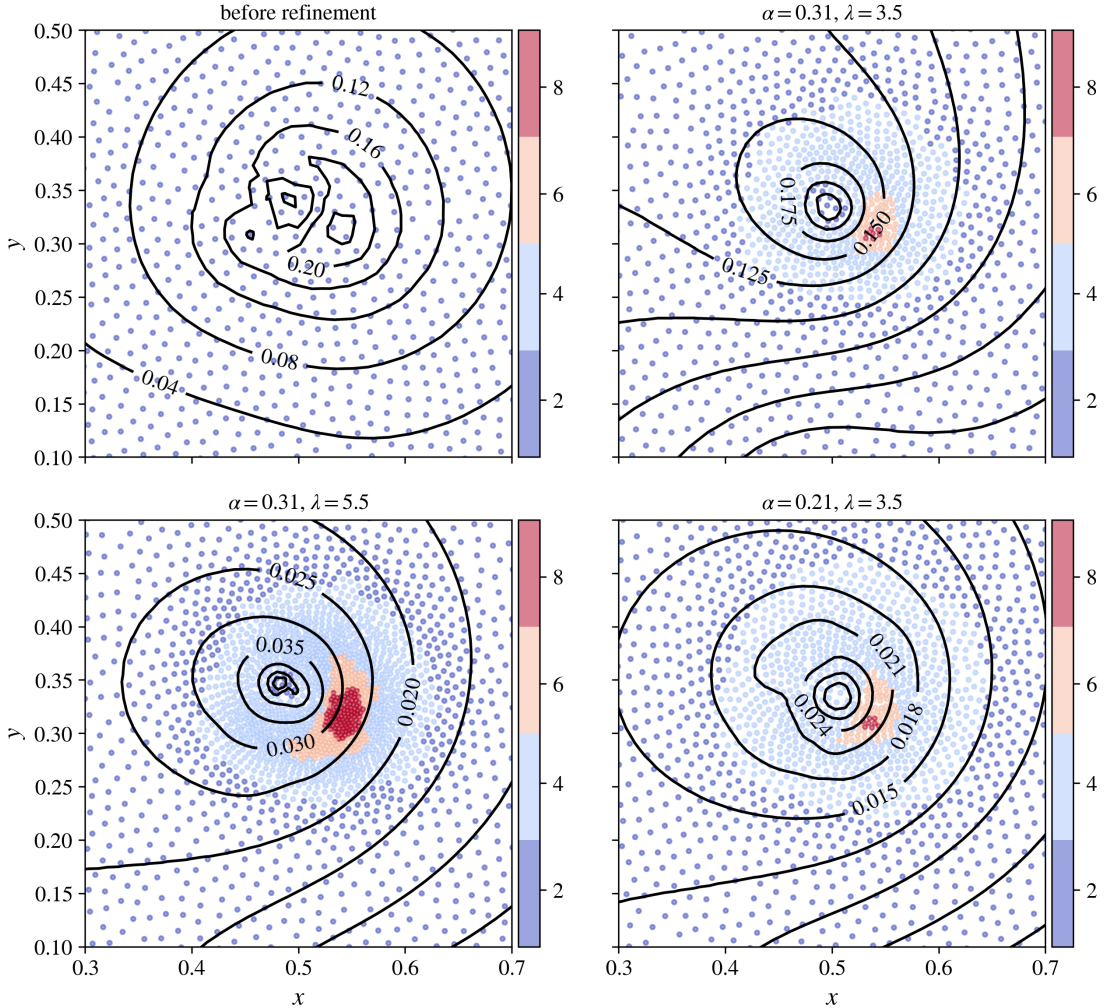


Figure 5: Demonstration of hp -refinement for selected values of refinement parameters. The top left figure shows the numerical solution before its refinement, while the rest show its refined state for different values of refinement parameters. Contour lines are used to show the absolute error of the numerical solution. To denote the p -refinement, the nodes are coloured according to the local approximation order. For clarity, all figures are zoomed to show only the neighbourhood of the strong source in the domain.

if α is too large, almost no refinement takes place and if it does, it is extremely local, which again has no beneficial consequences as it often leads to a violation of the quasi-uniform nodal distribution requirement.

It is therefore not straightforward to determine the optimal values for these parameters in advance. Fortunately, in our tests, the proposed solution procedure has proved to be stable enough so that a sufficiently good combination of all 8 parameters is not difficult to find. However, a thorough analysis of these parameters and their correlation is still needed, but is beyond the scope of this paper, whose aim is to present a *hp*-adaptive solution procedure in the context of mesh-free methods, rather than discussing optimal marking and refinement strategies. Nevertheless, we tried to reduce the number of free parameters by using the same values for *h*- and *p*-adaptivity (see Figure 5). While this approach also resulted in satisfactory results clearly outperforming the numerical solutions obtained with uniform nodal and approximation order distributions in terms of accuracy, significantly better results were easily obtained with the full 8 parameter formulation.

A step beyond the artificial refinement strategies. The refinement strategy could also be based on a specific knowledge about convergence rates and computational complexity in terms of internodal distance $h(p)$ and local approximation orders $m(p)$. From the convergence rates of unrefined solutions, we know that the error e is proportional to $h(p)^{m(p)}$. Knowing the target error e_t , we write the ratio of e_t/e_0 as

$$\frac{e_t}{e_0} \propto \frac{h^{m_t}}{h^{m_0}} = h^{m_t - m_0}, \quad (8)$$

where m_t is used to denote the target approximation order and m_0 is the current order of the approximation used to compute current error e_0 . From equation (8) a smarter guess for target local approximation order can be obtained

$$m_t = m_0 + \ln \frac{e_t}{e_0}. \quad (9)$$

Such strategy would conveniently leave the approximation order unchanged when $e_t = e_0$, increase it when $e_t < e_0$ and decrease it when $e_t > e_0$.

A step even further could be to additionally consider the change in computational complexity, similar to what the authors of [36] and [45] have already shown. Therefore, we believe that future work should consider the minimum local computational complexity criteria. A rough computational complexity can be obtained with the help of

$$\chi \propto \frac{\binom{m_t+d}{d}^3 \left(\frac{1}{h_t}\right)^d}{\binom{m_0+d}{d}^3 \left(\frac{1}{h_0}\right)^d}, \quad (10)$$

for domain dimensionality d and target and current internodal distances h_t and h_0 respectively.

2.7. Implementation note

The entire *hp*-adaptive solution procedure from Algorithm 1 is implemented in C++. All mesh-free methods and approaches used in this work are included in our in-house developed *Medusa library* [52]. The code¹ was compiled using g++ (GCC) 9.3.0 for Linux with -O3 -DNDEBUG -fopenmp flags. Post-processing was done using Python 3.10 and Jupyter notebooks, also available in the provided git repository.

3. Demonstration on exponential peak problem

The proposed *hp*-adaptive solution procedure is first demonstrated on a synthetic example. We chose a 2-dimensional Poisson problem with exponentially strong source positioned at $x_s = \left(\frac{1}{2}, \frac{1}{3}\right)$. This example is categorized as a difficult problem and is commonly used to test the performance of adaptive solution procedures [2, 43, 57, 30].

¹The source code is available at: https://gitlab.com/e62Lab/public/2022_p_hp-adaptivity under tag *v1.1*.

The problem has a tractable solution $u(\underline{x}) = e^{-a\|\underline{x}-\underline{x}_s\|^2}$, which allows us to evaluate the precision of the numerical solution \widehat{u} , e.g. in terms of the infinity norm

$$e_\infty = \frac{\|\widehat{u} - u\|_\infty}{\|u\|_\infty}, \quad \|u\|_\infty = \max_{i=1,\dots,N} |u_i|. \quad (11)$$

Governing equations are

$$\nabla^2 u(\underline{x}) = 2ae^{-a\|\underline{x}-\underline{x}_s\|^2} (2a\|\underline{x} - \underline{x}_s\| - d) \quad \text{in } \Omega, \quad (12)$$

$$u(\underline{x}) = e^{-a\|\underline{x}-\underline{x}_s\|^2} \quad \text{on } \Gamma_d, \quad (13)$$

$$\nabla u(\underline{x}) = -2a(\underline{x} - \underline{x}_s)e^{-a\|\underline{x}-\underline{x}_s\|^2} \quad \text{on } \Gamma_n, \quad (14)$$

for a d -dimensional domain Ω and strength $a = 10^3$ of the exponential source. The domain boundary is split into two sets: Neumann $\Gamma_n = \{\underline{x}, x \leq \frac{1}{2}\}$ and Dirichlet $\Gamma_d = \{\underline{x}, x > \frac{1}{2}\}$ boundaries. An example hp -refined numerical solution is shown in Figure 6.

In the continuation of this paper, the numerical solution of the final linear system is obtained by employing BiCGSTAB solver with a ILUT preconditioner from the Eigen C++ library [58]. Global tolerance was set to 10^{-15} with a maximum number of 300 iterations and drop-tolerance and fill-factor set to 10^{-5} and 50 respectively. While the initial adaptivity solution was obtained without the guess, all other iterations used the previous numerical solution \widehat{u}_{i-1} as the guess for new numerical solution \widehat{u}_i , effectively reducing the number of iterations required by the BiCGSTAB solver.

3.1. Convergence analysis of unrefined solution

The problem is first solved on a two-dimensional unit disc without employing any refinement procedures, i.e. with uniform nodal and approximation order distributions. The shapes approximating the linear differential operators are computed using the RBF-FD with PHS order $k = 3$ and monomial augmentation $m \in \{2, 4, 6, 8\}$.

Figure 7 shows the results. Each plotted point is an average obtained after 50 consecutive runs with slightly different domain discretisations (a random seed for generating expansion candidates was changed, see [51] for more details). In this way, we can not only study the convergence behaviour, but also evaluate how prone the numerical method is to non-optimal domain discretisations. The convergence of the numerical solution for selected monomial augmentations is shown on the left. We observe that due to the strong source, the convergence rates no longer follow the theoretical prediction of being proportional to h^m . Instead, the convergence rates for a small number of computational nodes ($N \lesssim 2000$) are significantly lower than that obtained for larger domain discretisations ($N \gtrsim 3000$) for all approximation orders $m > 2$. Furthermore, the accuracy gain by using higher order approximations with small domain discretisations is practically negligible. However, when the local field description is sufficient, both the numerical solution and the IMEX error indicator (Figure 7 on the right) give reliable results. While we could have forced at least one node in the neighbourhood of the source, we do not use any special techniques in this work. Instead, further research is simply limited to sufficiently large domains so that this observation does not represent an issue.

Moreover, the behaviour of the IMEX error indicator is studied on the right side of Figure 7. Here, the approximation order m means that the implicit numerical solution u^{im} was obtained with approximation order m , while the

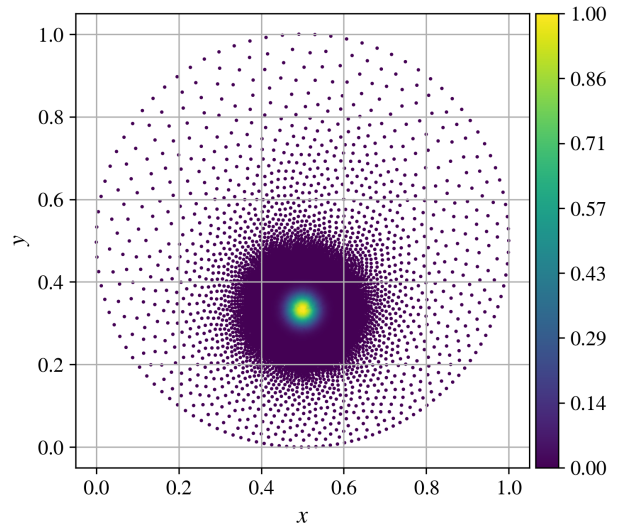


Figure 6: Example hp -refined solution to exponential peak problem.

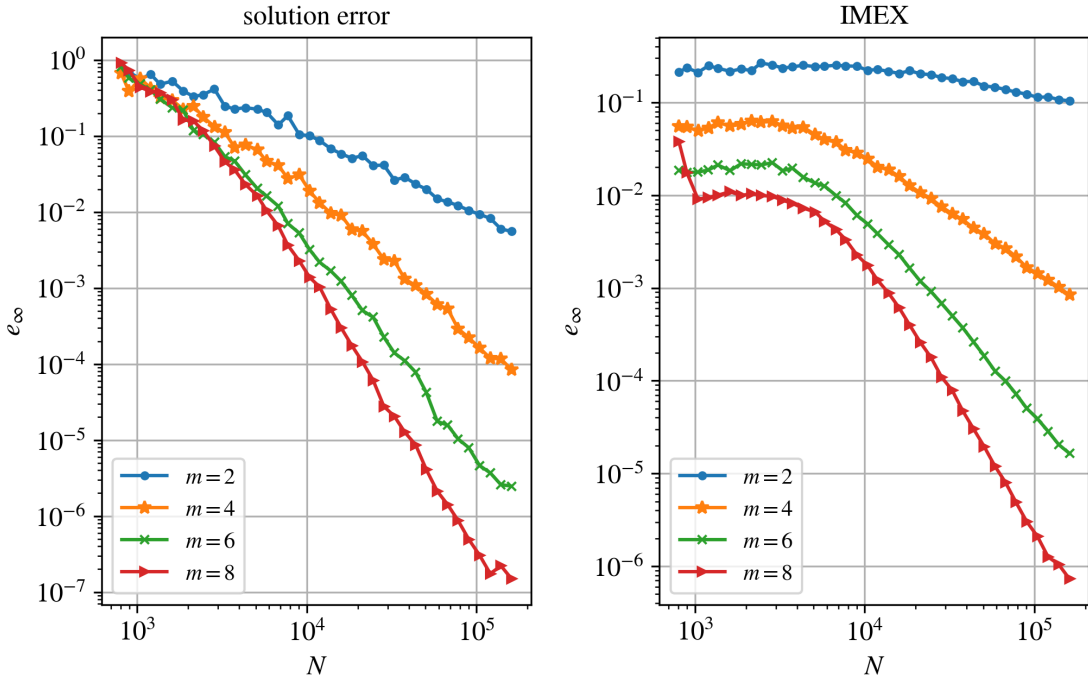


Figure 7: Convergence of unrefined numerical solution (left) and IMEX error indicator (right). Figure only shows a median value after 50 runs with slightly different domain discretisations. Note that, the approximation order m in the right figure denotes the approximation order used to obtain the numerical solution, while the explicit operators employed by the IMEX error indicator are approximated with orders $m + 2$.

explicit operators \mathcal{L}^{ex} from IMEX were approximated using monomials up to and including order $m + 2$. The observations show that the maximum value of the error indicator also converges with the number of computational nodes. Moreover, we can also observe the aforementioned change in the convergence rate of the numerical solution, since the maximum value of the error indicator for domain sizes $N \lesssim 3000$ is approximately constant.

3.2. Analysis of hp-refined solution

The same problem is now solved by employing the *hp*-adaptivity. Free parameters are adjusted to each refinement type, as can be seen in Table 1. Adaptivity iteration loop is stopped after a maximum of N_{iter} iterations. For practical use, other stopping criteria could also be used, e.g. based on the maximum error indicator reduction

$$\frac{\eta_{max}^j}{\eta_{max}^0} \leq \gamma, \quad (15)$$

for the iteration index j . The shapes are computed with RBF-FD using the PHS with order $k = 3$ and local monomial augmentation restricted to choose between approximation orders $m \in \{2, 4, 6, 8\}$. Note that the IMEX error indicator increases the local approximation order by 2, effectively using monomial orders $m_{IMEX} \in \{4, 6, 8, 10\}$. Furthermore, to avoid unreasonably large number of computational nodes, the maximum number of allowed nodes N_{max} is defined. Once this number is reached, further h -refinement is prevented and only de-refinement is allowed, while the p -adaptive method retains its full functionality. To avoid insufficient local field description, the local nodal density is limited by an upper bound, i.e. $h(p) \leq h_{max}$. The order of the PHS is left constant.

3.2.1. A brief analysis of IMEX error indicator

Figure 8 shows example indicator fields for the initial iteration, the intermediate iteration, and the iteration that achieved the best numerical solution accuracy – hereafter also referred to as the best-performing iteration or simply the best iteration. The third column shows the IMEX error indicator. We can see that the IMEX has successfully located

β_h	α_h	λ_h	ϑ_h	β_p	α_p	λ_p	ϑ_p	h_{max}	N_{max}	N_{iter}
0.175	0.225	2.625	1.01	10^{-4}	0.05	5	1.258	0.1	$2.5 \cdot 10^5$	70

Table 1: Adaptivity parameters used to obtain solution to the peak problem.

the position of the strong source at $\underline{x}_s = \left(\frac{1}{2}, \frac{1}{3}\right)$ as the highest indicator values are seen in its vicinity. Furthermore, the second column shows that both the accuracy of the numerical solution and the uniformity of the error distribution were significantly improved by the hp -adaptive solution procedure, further proving that IMEX can be successfully used as a reliable error indicator.

The behaviour of IMEX over 70 adaptivity iterations is also studied in Figure 9. We are pleased to find that the convergence limit of the indicator around iteration $N_{iter} = 60$ agrees well with the convergence limit of the numerical solution. This observation also makes the IMEX error indicator suitable for stopping criteria. Note that, in the process, the maximum error of the numerical solution has been reduced by about 9 orders of magnitude, while the maximum value of the error indicator has been reduced by about 7 orders of magnitude. In addition, Figure 9 also shows the number of computational nodes with respect to the adaptivity iterations.

3.2.2. Approximation order distribution

The iterative adaptive procedure starts by obtaining the numerical solution of the unrefined problem setup. In this step, the approximation with the lowest approximation order, i.e. $m = 2$, is assigned to all computational nodes. Later, the approximation orders are changed according to the marking and refinement strategies. Figure 8 shows the approximation order distributions for 3 selected adaptivity iterations. We can observe that the highest approximation orders are all near the exponentially strong source. Moreover, due to h -adaptivity, the node density in the neighbourhood of the strong source is also significantly increased, i.e. $h_{max}/h_{min} \approx 52$ in the best-performing iteration.

After applying the p -refinement strategy in the refinement step, the approximation order in two neighbouring nodes may differ by more than one. While numerical experiments with FEM have shown that heterogeneity of polynomial order in FEM leads to undesired oscillations of the approximated solution [59], no similar behaviour was observed in our analyses with our setup using mesh-free methods. Thus, in contrast to p -FEM, where additional smoothing of the approximation order takes place within the refinement module, we have completely avoided such manipulations and allow the approximation order in two neighbouring nodes to differ by more than one.

3.2.3. Convergence rates of hp -adaptive solution procedure

Finally, the convergence behaviour of the proposed hp -adaptive solution procedure is studied. In addition to the convergence of a single hp -adaptive run, Figure 10 shows the convergences obtained without the use of refinement procedures, i.e. solutions obtained with uniform internodal spacing and approximation orders over the entire domain. The figure clearly shows that a hp -adaptive solution procedure was able to significantly improve the numerical solution in terms of accuracy and computational points required.

As previously discussed by Eibner [35] and Demkowicz [37], we believe that a more complex marking and refinement strategies would further improve the convergence behaviour, but already the proposed hp -adaptive solution procedure significantly outperforms the unrefined solutions. Specifically, the refined solution is almost 4 orders of magnitude more accurate than the unrefined solution (for the highest approximation order $m = 8$ used) at about 10^4 computational nodes.

4. Application to linear elasticity problems

4.1. Fretting fatigue contact

The application of the proposed hp -adaptive solution procedure is further expanded to study a linear elasticity problem. Specifically, we obtain a hp -refined solution to fretting fatigue contact problem [60] for which no closed form solution is known.

The problem dynamics is governed by the Cauchy-Navier equations

$$(\lambda + \mu) \nabla(\nabla \cdot \underline{u}) + \mu \nabla^2 \underline{u} = \underline{f} \quad (16)$$

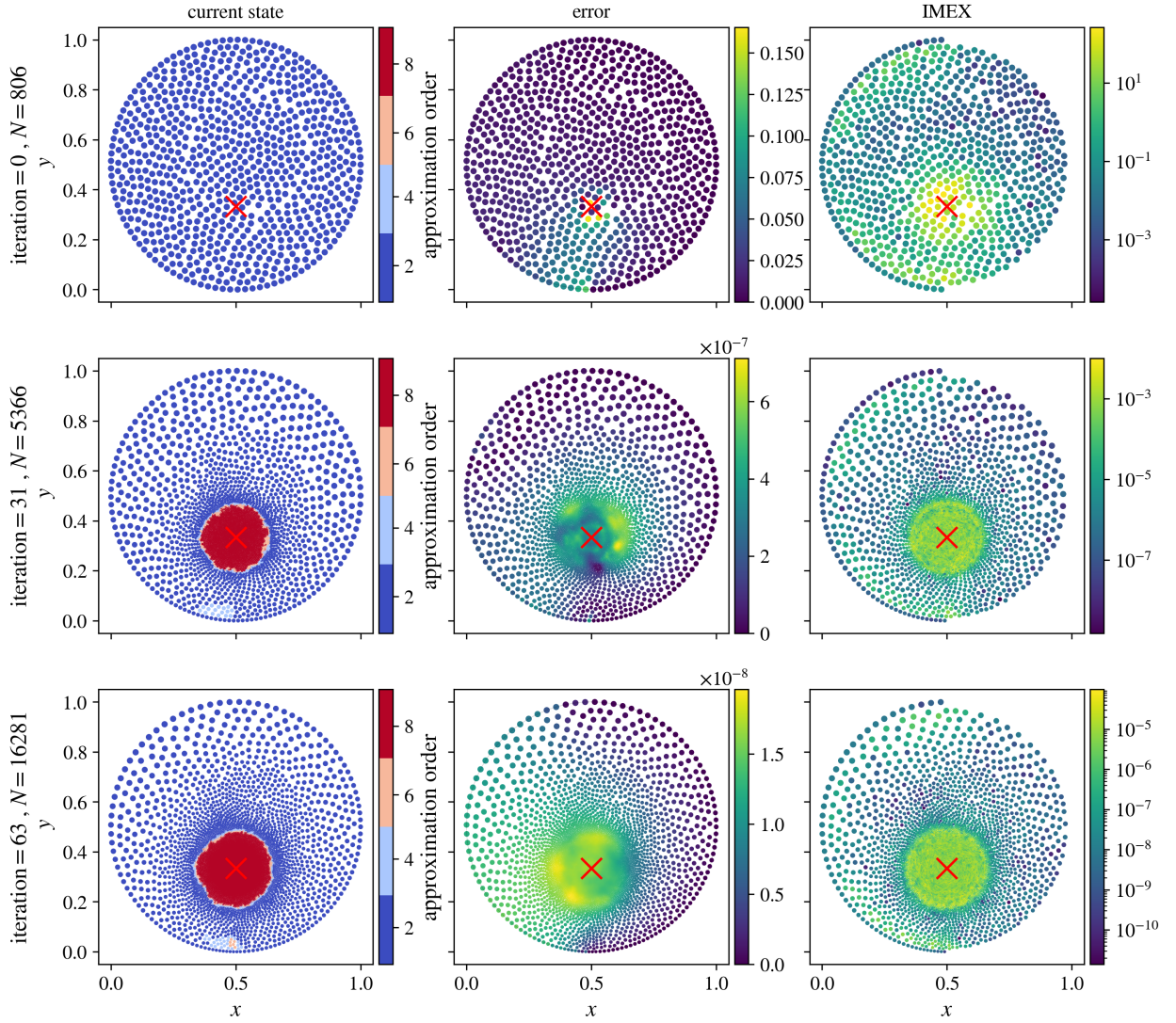


Figure 8: Refinement demonstration. Initial iteration (top row), intermediate iteration (middle row) and best-performing iteration (bottom row) accompanied with solution error (middle column) and IMEX error indicator values (right column). The IMEX values for Dirichlet boundary nodes are not shown. A red cross is used to mark the location of the strong peak.

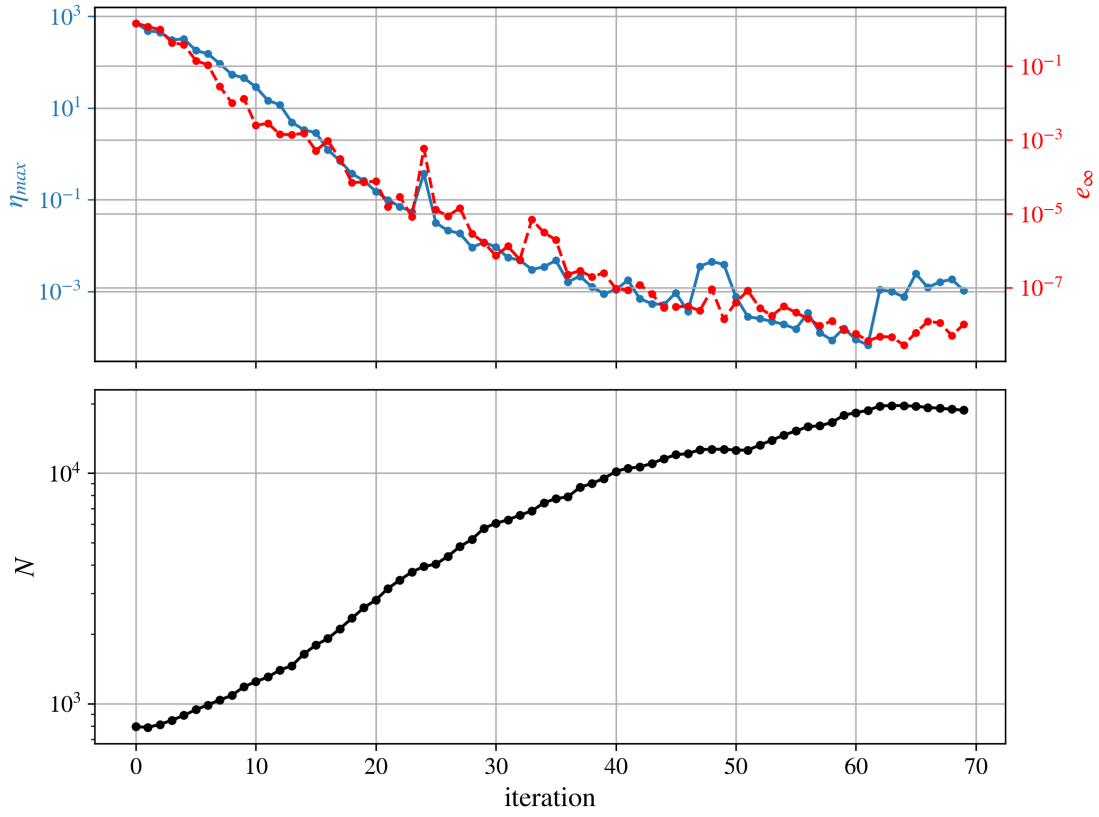


Figure 9: In the top row convergence of IMEX error indicator (blue) and convergence of numerical solution (red) within 70 iterations is shown, while the total number of computational nodes is shown below.

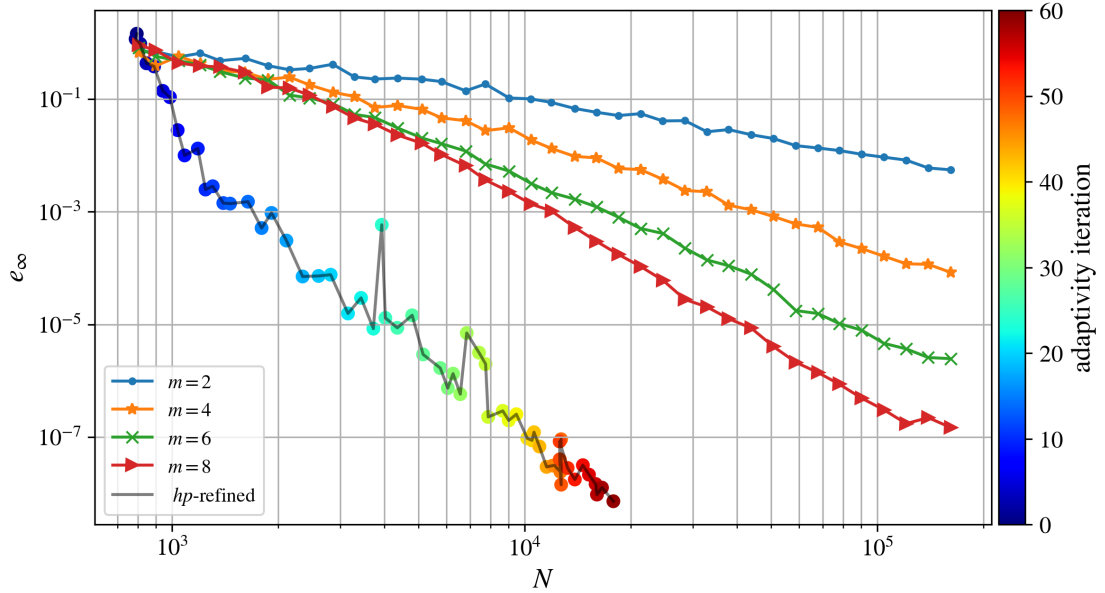


Figure 10: Convergence of the hp -refined solution compared to the convergence of the unrefined solutions.

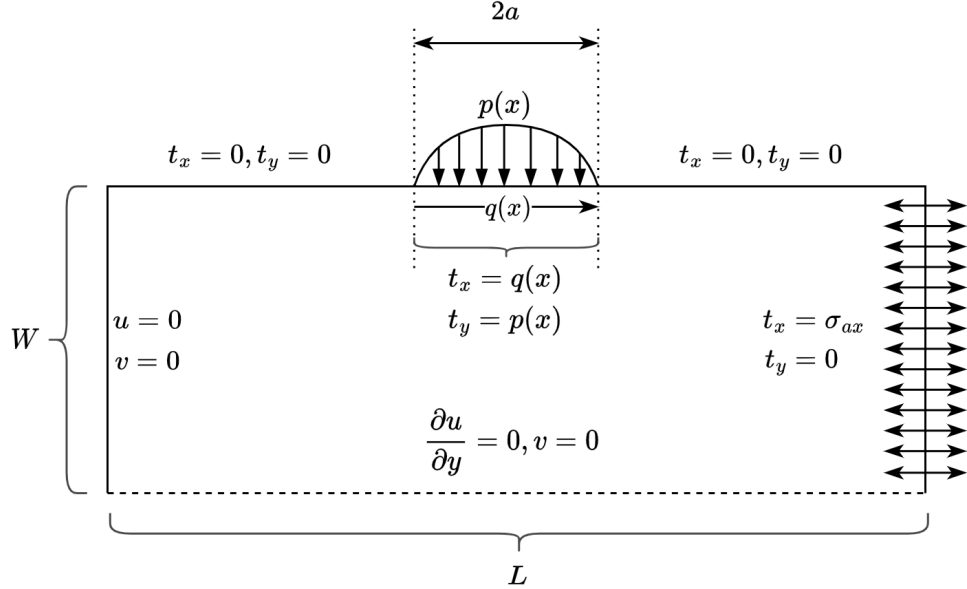


Figure 11: Fretting fatigue contact problem scheme and boundary conditions.

with unknown displacement vector \mathbf{u} , external body force \mathbf{f} and Lamé parameters μ and λ . The domain of interest is a thin rectangle of width W , length L and thickness D . Axial traction σ_{ax} is applied to the right side of the rectangle, while a compression force is applied to the centre of the rectangle to simulate contact. The contact is simulated by a compressing force F generated by two oscillating cylindrical pads of radius R , causing a tangential force Q . The tractions introduced by the two pads are predicted using an extension of Hertzian contact theory, which splits the contact area into the stick and slip zones depending on the friction coefficient μ and the combined elasticity modulus $E^{*-1} = \left(\frac{1-v_1^2}{E_1} + \frac{1-v_2^2}{E_2}\right)$, where E_i and v_i are the Young's modulus and the Poisson's ratios of the sample and the pad, respectively. The problem is shown schematically in Figure 11 together with the boundary conditions.

Theoretical predictions from [11] are used to obtain the contact half-width

$$a = 2 \sqrt{\frac{FR}{t\pi E^*}}, \quad (17)$$

with normal traction

$$p(x) = \begin{cases} p_0 \sqrt{1 - \frac{x^2}{a^2}}, & |x| < a \\ 0, & \text{else} \end{cases}, \quad p_0 = \sqrt{\frac{FE^*}{t\pi R}}, \quad (18)$$

and tangential traction

$$q(x) = \begin{cases} -\mu p_0 \left(\sqrt{1 - \frac{x^2}{a^2}} - \frac{c}{a} \sqrt{1 - \frac{(x-e)^2}{c^2}} \right), & |x - e| < c \\ -\mu p_0 \sqrt{1 - \frac{x^2}{a^2}}, & c \leq |x - e| \text{ and } |x| \leq a \\ 0, & \text{else} \end{cases} \quad (19)$$

for $c = a \sqrt{1 - \frac{Q}{\mu F}}$ defined as the half-width of the slip zone and $e = \text{sgn}(Q) \frac{a\sigma_{ax}}{4\mu p_0}$ is the eccentricity due to axial loading. Note that the inequalities $Q \leq \mu F$ and $\sigma_{ax} \leq 4 \left(1 - \sqrt{1 - \frac{Q}{\mu F}}\right)$ must hold for these expressions to be valid.

Plane strain approximation is used to reduce the problem from three to two dimensions and symmetry along the horizontal axis is used to further halve the problem size. Finally, $\Omega = [-L/2, L/2] \times [-W/2, 0]$ is taken as the domain.

β_h	α_h	λ_h	ϑ_h	β_p	α_p	λ_p	ϑ_p	h_{max}	N_{max}	N_{iter}
$5 \cdot 10^{-5}$	10^{-4}	5	1.051	10^{-3}	10^{-1}	4	1.051	$2.5 \cdot 10^{-4}$	$5 \cdot 10^5$	19

Table 2: Adaptivity parameters used to obtain solution to fretting fatigue contact problem.

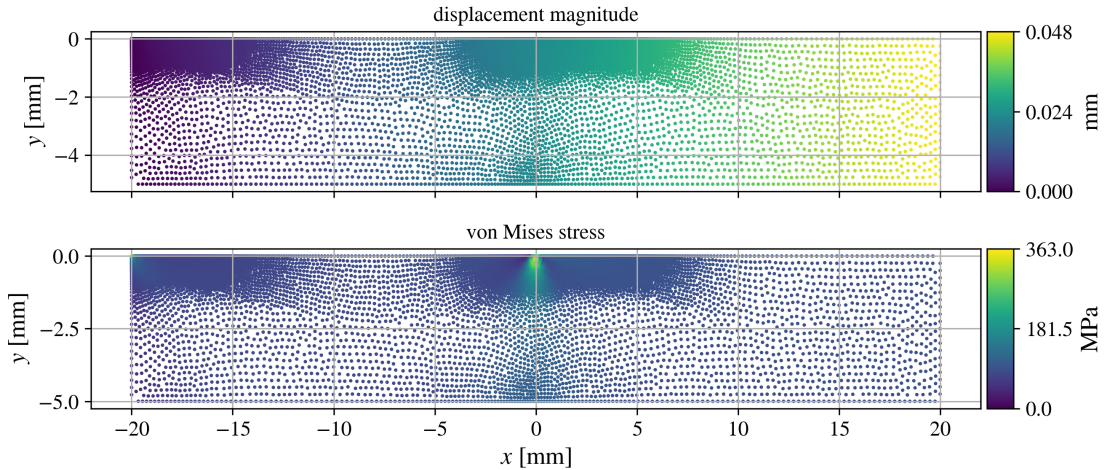


Figure 12: Example hp -refined fretting fatigue contact solution.

We take $E_1 = E_2 = 72.1$ GPa, $\nu_1 = \nu_2 = 0.33$, $L = 40$ mm, $W = 10$ mm, $t = 4$ mm, $F = 543$ N, $Q = 155$ N, $\sigma_{ax} = 100$ MPa, $R = 10$ mm and $\mu = 0.3$ for the model parameters. With this setup, the half-contact width a is equal to 0.2067 mm, which is about 200 times smaller than the domain width W . For stability reasons, the 4 corner nodes were removed after the domain was discretised.

The linear differential operators are approximated with RBF-FD using the PHS with order $k = 3$ and local monomial augmentation limited to choose between approximation orders $m \in \{2, 4, 6, 8\}$. The PHS order was left constant during the adaptive refinement. The hp -refinement parameters used to obtain the numerical solution are given in Table 2.

Figure 12 shows an example of a hp -refined solution to fretting fatigue problem in the last adaptivity iteration with $N = 46\,626$ computational nodes. We see that the solution procedure has successfully located the two critical points, i.e. the fixed upper left corner with a stress singularity and the area in the middle of the upper edge where contact is simulated. Note that the highest stress values (about 2 times higher) were calculated in the singularity in the upper left corner, but these nodes are not shown as our focus is shifted towards the area under the contact.

4.1.1. Surface traction under the contact

For a detailed analysis, we consider the surface traction σ_{xx} , as it is often used to determine the location of crack initiation. The surface traction is shown in Figure 13 for 6 selected adaptivity iterations. The mesh-free nodes are coloured according to the local approximation order enforced by the hp -adaptive solution procedure. The message of this figure is twofold. First, it is clear that the proposed IMEX error indicator can be successfully used in linear elasticity problems, and second, we find that the hp -adaptive solution procedure has successfully approximated the surface traction near the contact. In doing so, the local field description under the contact has been significantly improved and the local approximation orders have taken a non-trivial distribution.

The surface traction in Figure 13 is additionally accompanied with the FEM results on a much denser mesh with more than 100 000 DOFs obtained with the commercial solver Abaqus[®] [60]. To calculate the absolute difference between the two methods, the mesh-free solution was interpolated to Abaqus's computational points using Sheppard's inverse distance weighting interpolation with 2 nearest neighbours. We see that the absolute difference under the contact decreases with the number of adaptivity iterations and eventually settles at approximately 2 % of the maximum difference from the initial iteration. As expected, the highest absolute difference is at the edges of the contact, i.e.

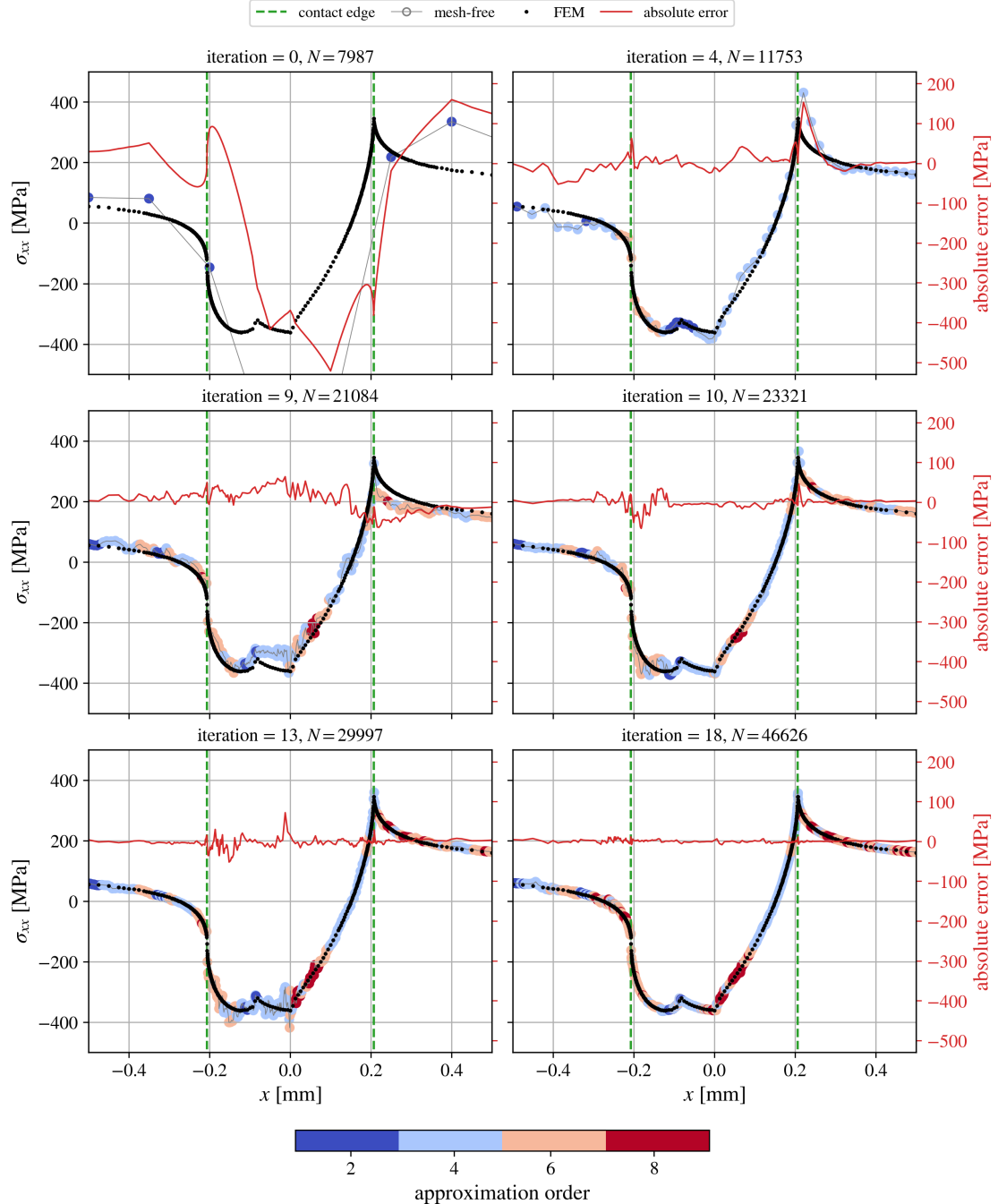


Figure 13: Surface traction under the contact for selected iteration steps demonstrating the hp -adaptivity process. Colours are used to denote the local approximation orders. Numerical solution is additionally compared against the Abaqus FEM solution, where the red line is used to denote the absolute difference between the two methods. For clarity, the two dashed green lines show the edge contact.

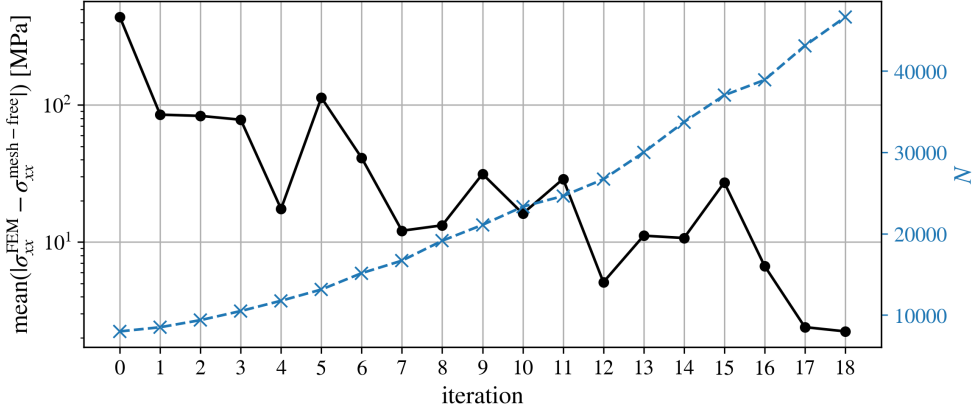


Figure 14: Mean surface traction difference between the two methods under the contact area.

around $x = a$ and $x = -a$, while the difference is even smaller in the rest of the contact area. The absolute difference between the two methods is further studied in Figure 14, where the mean of $|\sigma_{xx}^{FEM} - \sigma_{xx}^{\text{mesh-free}}|$ under the contact area, i.e. $-a \leq x \leq a$, is shown. We observe that the mesh-free hp -refined solution converges towards the reference FEM solution with respect to the adaptivity iterations. Moreover, Figure 14 also shows the number of computational nodes with respect to the adaptivity iteration.

4.2. The three-dimensional Boussinesq's problem

As a final benchmark problem we solve the three-dimensional Boussinesq's problem, where a concentrated normal traction acts on an isotropic half-space [61].

The problem has a closed form solution given in cylindrical coordinates r , θ and z as

$$\begin{aligned}
 u_r &= \frac{Pr}{4\pi\mu} \left(\frac{z}{R^3} - \frac{1-2\nu}{R(z+R)} \right), & u_\theta &= 0, & u_z &= \frac{P}{4\pi\mu} \left(\frac{2(1-\nu)}{R} + \frac{z^2}{R^3} \right), \\
 \sigma_{rr} &= \frac{P}{2\pi} \left(\frac{1-2\nu}{R(z+R)} - \frac{3r^2z}{R^5} \right), & \sigma_{\theta\theta} &= \frac{P(1-2\nu)}{2\pi} \left(\frac{z}{R^3} - \frac{1}{R(z+R)} \right), \\
 \sigma_{zz} &= -\frac{3Pz^3}{2\pi R^5}, & \sigma_{rz} &= -\frac{3Prz^2}{2\pi R^5}, & \sigma_{r\theta} &= 0, & \sigma_{\theta z} &= 0,
 \end{aligned} \tag{20}$$

where P is the magnitude of the concentrated force, ν is the Poisson's ratio, μ is the Lamé parameter and R is the Euclidian distance to the origin. The solution has a singularity at the origin, which makes the problem ideal for treatment with adaptive procedures. Furthermore, the closed form solution also allows us to evaluate the accuracy of the numerical solution.

In our setup, we consider only a small part of the problem, i.e. $\varepsilon = 0.1$ away from the singularity, as schematically shown in Figure 15. From a numerical point of view, we solve the Navier-Cauchy equation (16) with Dirichlet boundary conditions described in (20), where the domain Ω is defined as a box, i.e. $\Omega = [-1, -\varepsilon] \times [-1, -\varepsilon] \times [-1, -\varepsilon]$.

Although the closed form solution is given in cylindrical coordinate systems, the problem is implemented using cartesian coordinates. We employ the proposed

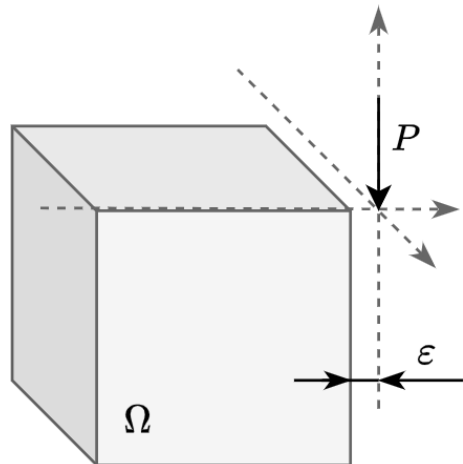


Figure 15: Schematic presentation of Boussinesq's problem.

β_h	α_h	λ_h	ϑ_h	β_p	α_p	λ_p	ϑ_p	h_{max}	N_{max}	N_{iter}
10^{-3}	10^{-3}	3.75	1.01	10^{-4}	10^{-2}	3	1.5	0.04	$7 \cdot 10^4$	20

Table 3: Adaptivity parameters used to obtain solution to Boussinesq's problem.

displacement magnitude

von Mises stress

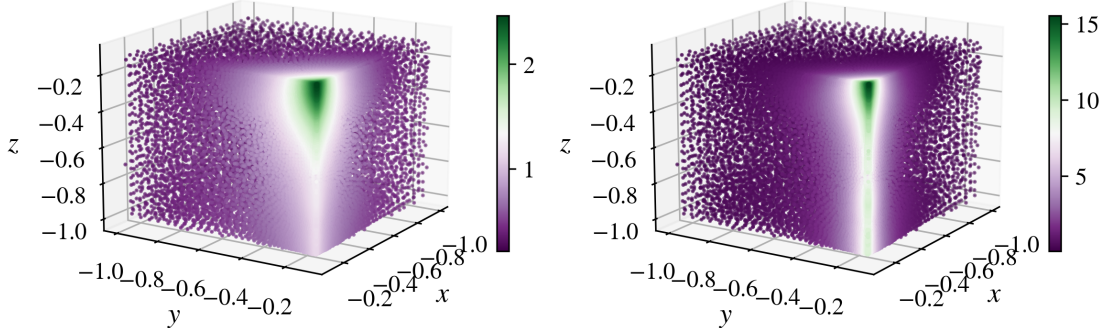


Figure 16: Example hp -refined numerical solution to Boussinesq's problem.

mesh-free hp -adaptive solution procedure where the shapes are computed with RBF-FD using the PHS with order $k = 3$ and monomial augmentation restricted to choose between approximation orders $m \in \{2, 4, 6, 8\}$. Other hp -refinement related parameters are given in Table 3. For the physical parameters of the problem, the values $P = -1$, $E = 1$ and $\nu = 0.33$ were assumed.

Example hp -refined numerical solution is given in Figure 16. We can see that the proposed hp -adaptive solution procedure is sufficiently robust to obtain a good solution even for three-dimensional problems with singularities. Additionally, we also observe that the IMEX error indicator successfully identified the singularity, effectively seen as an increase in the local field description in the neighbourhood of the concentrated force applied at the origin.

4.2.1. The von Mises stress along the body diagonal

Figure 17 shows further evaluation of the hp -refined mesh-free numerical solution. Here, the von Mises stress at points near the body diagonal $(-1, -1, -1) \rightarrow (-\varepsilon, -\varepsilon, -\varepsilon)$ is calculated for selected 4 adaptivity iterations and compared to the analytical values in terms of relative error. In addition, the nodes are coloured according to the local approximation order enforced by the hp -adaptive solution procedure. We can see that the highest relative error of approximately 0.3 at the initial state is observed in the neighbourhood of the origin. In the final iteration, the relative error is reduced by about an order of magnitude. We also see that the hp -adaptive solution procedure has found a non-trivial order distribution and that the number of nodes in the neighbourhood of the corner $(-\varepsilon, -\varepsilon, -\varepsilon)$ has increased significantly.

A more quantitative analysis of the mesh-free solution is given in Figure 18 where the ℓ_1 , ℓ_2 and ℓ_∞ error norms and number of computational nodes vs. adaptivity iteration are shown. Compared to the initial state, the hp -adaptive solution procedure was able to achieve a numerical solution that was almost two orders of magnitude more accurate. In the process, the number of computational nodes increased from 10 500 in the initial state to about 80 000 in the final iteration. However, it is interesting to observe that with the configuration from Table 3, none of the computational nodes used the approximation with the highest order allowed ($m = 8$). Instead, in the final iteration, there were 130 nodes approximated with $m = 6$, and 5937 with $m = 4$, while the rest were approximated with the second order. Note that, as expected, most of the higher order approximations are near the concentrated force – which is difficult to represent visually, so we only give the descriptive data.

For reference, we take the h -refined solution by Slak et al. [11], who were able to reduce the infinity norm error by about an order of magnitude with $N \approx 140 000$ nodes in the final iteration. It is perhaps naive to compare this result

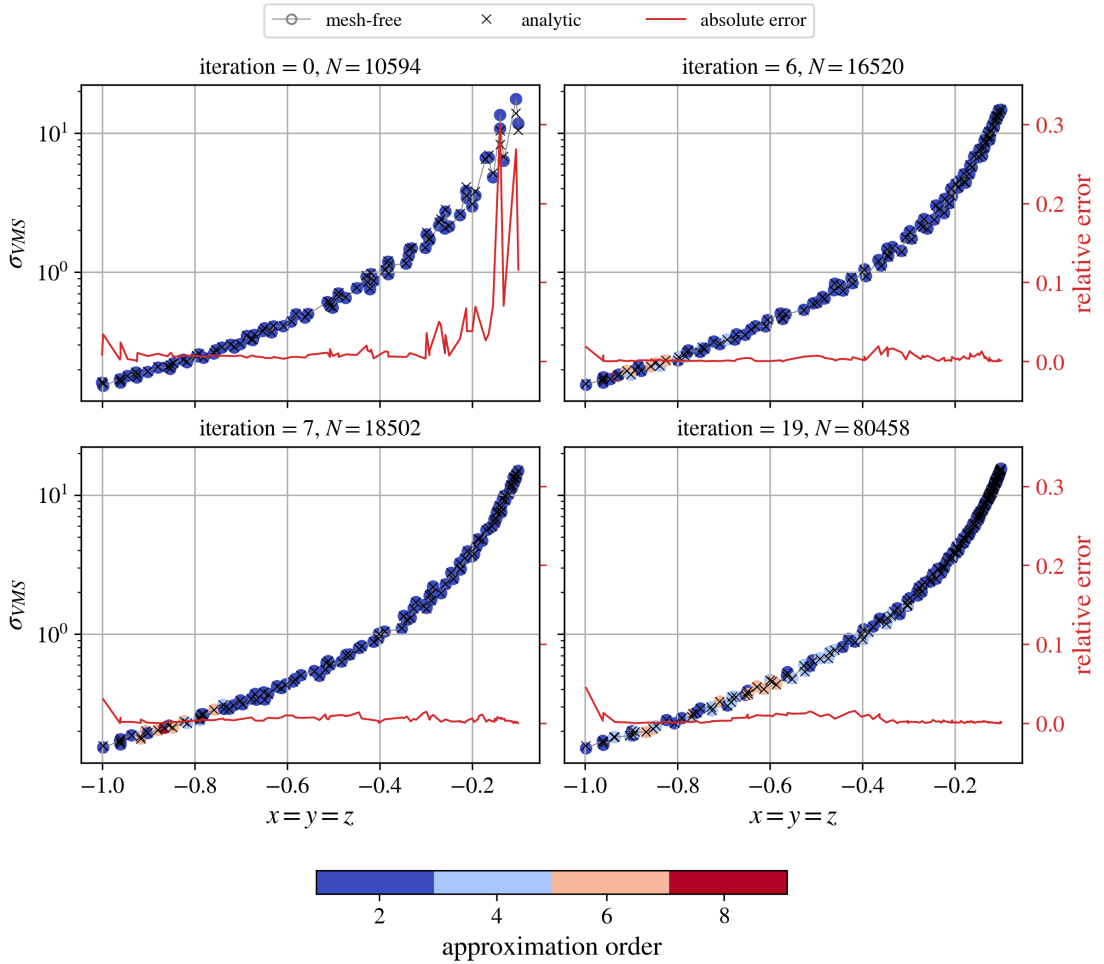


Figure 17: Numerical solution compared to analytical solution at the nodes near the body diagonal $(-1, -1, -1) \rightarrow (-\varepsilon, -\varepsilon, -\varepsilon)$ for selected iterations.

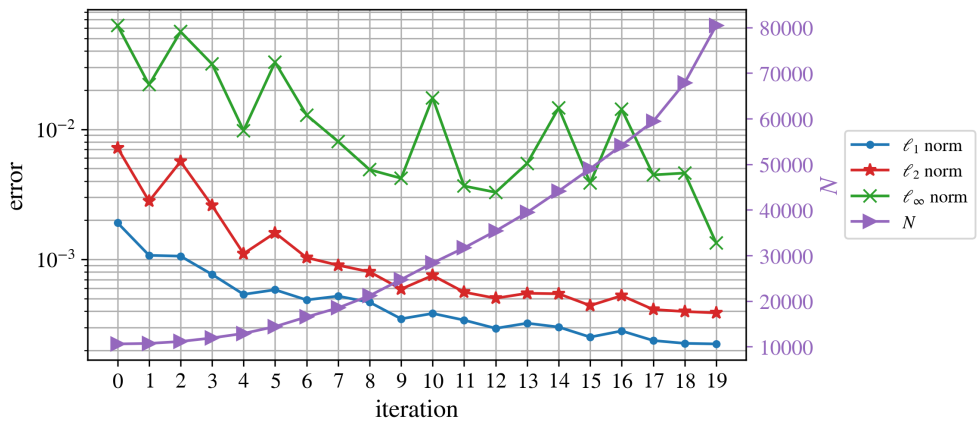


Figure 18: Convergence of numerical solution along with number of computational nodes.

with ours, since the authors use different marking and refinement strategies and, more importantly, a different error indicator. Nevertheless, the infinity norm error of our hp -refined solution is in the neighbourhood of 10^{-3} compared to theirs at approximately 10^{-2} with almost twice as many computational nodes. We believe our results could be further improved by fine-tuning the free parameters, but we decided to avoid such an approach.

5. Conclusions

In this paper we establish a baseline for hp strong form mesh-free analysis. We have formulated and implemented a hp -adaptive solution procedure and demonstrated its performance in three different numerical experiments.

The cornerstone of the presented hp -adaptive method is an iterative solve–estimate–mark–refine paradigm with the modified Texas Three Step marking strategy. The h -refine of the proposed method relies on an advancing front node positioning algorithm based on Poisson disc sampling, which enables dimension-independent node generation supporting spatially variable density distributions. For the adaptive order of the method, we exploit an elegant control over the order of the approximation via the augmenting monomials in the approximation basis.

We proposed an IMEX error indicator, where the implicit solution of the problem is processed with the higher order local explicit representation of PDE at hand, e.g. if the implicit solution is computed with a second order approximation, the explicit re-evaluation happens at fourth order. Our analyses show that the proposed error indicator successfully captures main characteristics of error distributions, which suffices for the proposed iterative adaptivity. The proposed hp -adaptive solution procedure is first demonstrated on a two-dimensional Poisson problem with exponential source and mixed boundary conditions. Further demonstration focuses on linear elasticity problems. First, a 2D fretting fatigue problem – a contact problem with pronounced peaks in the surface stress, and second, a 3D Boussinesq's problem with stress singularity. In both cases, we have demonstrated the advantages of using the proposed hp -adaptive approach.

Although we have observed a stable and convergent behaviour of the proposed solution procedure, we are aware that there are many opportunities for improvement. The IMEX error indicator needs further clarification. Other error indicators should also be implemented and tested. During our experiments, we have found that a marking strategy with more free parameters leads to better accuracy, but is also more difficult to understand and control and can be case dependent. A smarter and more effective refinement and marking strategies are certainly part of future work. These should possibly take into account more information about the method itself, e.g. the dependence of the computational complexity on the approximation order.

Acknowledgments

This work was supported by the ARRS research core funding No. P2-0095 and research project J2-3048. The authors would also like to thank Miha Rot for several fruitful discussions.

References

- [1] B. D. Upadhyay, S. S. Sonigra, S. D. Daxini, Numerical analysis perspective in structural shape optimization: A review post 2000, *Advances in Engineering Software* 155 (2021) 102992.
- [2] W. F. Mitchell, M. A. McClain, A comparison of hp -adaptive strategies for elliptic partial differential equations, *ACM Transactions on Mathematical Software (TOMS)* 41 (1) (2014) 1–39.
- [3] K. Segeth, A review of some a posteriori error estimates for adaptive finite element methods, *Mathematics and Computers in Simulation* 80 (8) (2010) 1589–1600, eSCO 2008 Conference. doi:<https://doi.org/10.1016/j.matcom.2008.12.019>.
URL <https://www.sciencedirect.com/science/article/pii/S0378475408004230>
- [4] G.-R. Liu, Y.-T. Gu, An introduction to meshfree methods and their programming, Springer Science & Business Media, 2005.
- [5] G.-R. Liu, Mesh free methods: moving beyond the finite element method, CRC press, 2002. doi:[10.1201/9781420040586](https://doi.org/10.1201/9781420040586).
- [6] O. C. Zienkiewicz, R. L. Taylor, J. Z. Zhu, The finite element method: its basis and fundamentals, Elsevier, 2005.
- [7] K. van der Sande, B. Fornberg, Fast variable density 3-d node generation, *SIAM Journal on Scientific Computing* 43 (1) (2021) A242–A257.
- [8] V. Shankar, R. M. Kirby, A. L. Fogelson, Robust node generation for mesh-free discretizations on irregular domains and surfaces, *SIAM Journal on Scientific Computing* 40 (4) (2018) A2584–A2608.
- [9] P. Suchde, T. Jacquemin, O. Davydov, Point Cloud Generation for Meshfree Methods: An Overview, *Archives of Computational Methods in Engineering* (Sep. 2022). doi:[10.1007/s11831-022-09820-w](https://doi.org/10.1007/s11831-022-09820-w).
URL <https://link.springer.com/10.1007/s11831-022-09820-w>

[10] T. Jacquemin, P. Suchde, S. P. Bordas, Smart Cloud Collocation: Geometry-Aware Adaptivity Directly From CAD, *Computer-Aided Design* 154 (2023) 103409. doi:10.1016/j.cad.2022.103409.
URL <https://linkinghub.elsevier.com/retrieve/pii/S0010448522001427>

[11] J. Slak, G. Kosec, Adaptive radial basis function-generated finite differences method for contact problems, *International Journal for Numerical Methods in Engineering* 119 (7) (2019) 661–686.

[12] O. Davydov, D. T. Oanh, Adaptive meshless centres and rbf stencils for poisson equation, *Journal of Computational Physics* 230 (2) (2011) 287–304.

[13] T. Jacquemin, S. P. A. Bordas, A unified algorithm for the selection of collocation stencils for convex, concave, and singular problems, *International Journal for Numerical Methods in Engineering* 122 (16) (2021) 4292–4312.

[14] M. Jančič, J. Slak, G. Kosec, Monomial augmentation guidelines for rbf-fd from accuracy versus computational time perspective, *Journal of Scientific Computing* 87 (1) (2021) 1–18.

[15] V. Bayona, N. Flyer, B. Fornberg, G. A. Barnett, On the role of polynomials in rbf-fd approximations: II. numerical solution of elliptic pdes, *Journal of Computational Physics* 332 (2017) 257–273.

[16] T. Belytschko, Y. Krongauz, D. Organ, M. Fleming, P. Krysl, Meshless methods: an overview and recent developments, *Computer methods in applied mechanics and engineering* 139 (1-4) (1996) 3–47.

[17] G. Kosec, B. Šarler, Simulation of macrosegregation with mesosegregates in binary metallic casts by a meshless method, *Engineering Analysis with Boundary Elements* 45 (2014) 36–44. doi:10.1016/j.enganabound.2014.01.016.
URL <https://linkinghub.elsevier.com/retrieve/pii/S0955799714000290>

[18] M. Maksić, V. Djurica, A. Souvent, J. Slak, M. Depolli, G. Kosec, Cooling of overhead power lines due to the natural convection, *International Journal of Electrical Power & Energy Systems* 113 (2019) 333–343. doi:10.1016/j.ijepes.2019.05.005.
URL <https://linkinghub.elsevier.com/retrieve/pii/S0142061518340055>

[19] W.-z. Gui, I. Babuška, The h, p and hp versions of the finite element method in 1 dimension. part 3. the adaptive hp version., Tech. rep., MARYLAND UNIV COLLEGE PARK LAB FOR NUMERICAL ANALYSIS (1985).

[20] W.-Z. Gui, I. Babuška, The h, p and hp versions of the finite element method in 1 dimension. part ii. the error analysis of the h and hp versions, *Numerische Mathematik* 49 (6) (1986) 613–657.

[21] P. R. Devloo, C. M. Bravo, E. C. Rylo, Recent developments in hp adaptive refinement.

[22] O. C. Zienkiewicz, J. Z. Zhu, A simple error estimator and adaptive procedure for practical engineering analysis, *International journal for numerical methods in engineering* 24 (2) (1987) 337–357.

[23] O. A. González-Estrada, S. Natarajan, J. J. Ródenas, S. P. Bordas, Error estimation for the polygonal finite element method for smooth and singular linear elasticity, *Computers & Mathematics with Applications* 92 (2021) 109–119.

[24] M. Thimnejad, N. Fallah, A. R. Khoei, Adaptive refinement in the meshless finite volume method for elasticity problems, *Computers & Mathematics with Applications* 69 (12) (2015) 1420–1443. doi:10.1016/j.camwa.2015.03.023.

[25] A. Angulo, L. P. Pozo, F. Perazzo, A posteriori error estimator and an adaptive technique in meshless finite points method, *Engineering Analysis with Boundary Elements* 33 (11) (2009) 1322–1338. doi:10.1016/j.enganabound.2009.06.004.

[26] D. T. Oanh, O. Davydov, H. X. Phu, Adaptive rbf-fd method for elliptic problems with point singularities in 2d, *Applied Mathematics and Computation* 313 (2017) 474–497.

[27] P. Sang-Hoon, K. Kie-Chan, Y. Sung-Kie, A posterior error estimates and an adaptive scheme of least-squares meshfree method, *International Journal for Numerical Methods in Engineering* 58 (8) (2003) 1213–1250. doi:10.1002/nme.817.

[28] M. Afshar, M. Naisipour, J. Amani, Node moving adaptive refinement strategy for planar elasticity problems using discrete least squares meshless method, *Finite Elements in Analysis and Design* 47 (12) (2011) 1315–1325.

[29] B. Guo, I. Babuška, The hp version of the finite element method, *Computational Mechanics* 1 (1) (1986) 21–41.

[30] W. F. Mitchell, Performance of hp-adaptive strategies for 3d elliptic problems (2016).

[31] J. Tinsley Oden, W. Wu, M. Ainsworth, Three-step hp adaptive strategy for the incompressible navier-stokes equations, in: *Modeling, mesh generation, and adaptive numerical methods for partial differential equations*, Springer, 1995, pp. 347–366.

[32] M. Ainsworth, B. Senior, Aspects of an adaptive hp-finite element method: Adaptive strategy, conforming approximation and efficient solvers, *Computer Methods in Applied Mechanics and Engineering* 150 (1-4) (1997) 65–87.

[33] P. Houston, B. Senior, E. Süli, Sobolev regularity estimation for hp-adaptive finite element methods, in: *Numerical mathematics and advanced applications*, Springer, 2003, pp. 631–656.

[34] P. Houston, E. Süli, A note on the design of hp-adaptive finite element methods for elliptic partial differential equations, *Computer Methods in Applied Mechanics and Engineering* 194 (2-5) (2005) 229–243.

[35] T. Eibner, J. M. Melenk, An adaptive strategy for hp-fem based on testing for analyticity, *Computational Mechanics* 39 (5) (2007) 575–595.

[36] M. Bürg, W. Dörfler, Convergence of an adaptive hp finite element strategy in higher space-dimensions, *Applied numerical mathematics* 61 (11) (2011) 1132–1146.

[37] L. Demkowicz, W. Rachowicz, P. Devloo, A fully automatic hp-adaptivity, *Journal of Scientific Computing* 17 (1) (2002) 117–142.

[38] W. Rachowicz, D. Pardo, L. Demkowicz, Fully automatic hp-adaptivity in three dimensions, *Computer methods in applied mechanics and engineering* 195 (37-40) (2006) 4816–4842.

[39] J. Benito, F. Urena, L. Gavete, R. Alvarez, An h-adaptive method in the generalized finite differences, *Computer methods in applied mechanics and engineering* 192 (5-6) (2003) 735–759.

[40] G. Liu, B. B. Kee, L. Chun, A stabilized least-squares radial point collocation method (ls-rpcm) for adaptive analysis, *Computer methods in applied mechanics and engineering* 195 (37-40) (2006) 4843–4861.

[41] W. Hu, N. Trask, X. Hu, W. Pan, A spatially adaptive high-order meshless method for fluid–structure interactions, *Computer Methods in Applied Mechanics and Engineering* 355 (2019) 67–93.

[42] A. Tolstykh, D. Shirobokov, On using radial basis functions in a “finite difference mode” with applications to elasticity problems, *Computational Mechanics* 33 (1) (2003) 68–79.

[43] D. T. Oanh, N. M. Tuong, An approach to adaptive refinement for the rbf-fd method for 2d elliptic equations, *Applied Numerical Mathematics*

178 (2022) 123–154.

- [44] L. Fan, Adaptive meshless point collocation methods: investigation and application to geometrically non-linear solid mechanics, Ph.D. thesis, Durham University (2019).
- [45] P. K. Mishra, L. Ling, X. Liu, M. K. Sen, Adaptive radial basis function generated finite-difference (rbf-fd) on non-uniform nodes using p -refinement, arXiv preprint arXiv:2004.06319 (2020).
- [46] S. Milewski, Higher order schemes introduced to the meshless fdm in elliptic problems, *Engineering Analysis with Boundary Elements* 131 (2021) 100–117.
- [47] A. Albuquerque-Ferreira, M. Ureña, H. Ramos, The generalized finite difference method with third-and fourth-order approximations and treatment of ill-conditioned stars, *Engineering Analysis with Boundary Elements* 127 (2021) 29–39.
- [48] T. Liszka, C. Duarte, W. Tworzydlo, hp-meshless cloud method, *Computer Methods in Applied Mechanics and Engineering* 139 (1-4) (1996) 263–288.
- [49] M. Jančič, J. Slak, G. Kosec, p-refined rbf-fd solution of a poisson problem, in: 2021 6th International Conference on Smart and Sustainable Technologies (SpliTech), 2021, pp. 01–06. doi:10.23919/SpliTech52315.2021.9566401.
- [50] C. A. Duarte, J. T. Oden, An hp adaptive method using clouds, *Computer methods in applied mechanics and engineering* 139 (1-4) (1996) 237–262.
- [51] J. Slak, G. Kosec, On generation of node distributions for meshless pde discretizations, *SIAM journal on scientific computing* 41 (5) (2019) A3202–A3229.
- [52] J. Slak, G. Kosec, Medusa: A c++ library for solving pdes using strong form mesh-free methods, *ACM Transactions on Mathematical Software (TOMS)* 47 (3) (2021) 1–25.
- [53] M. Depolli, J. Slak, G. Kosec, Parallel domain discretization algorithm for RBF-FD and other meshless numerical methods for solving PDEs, *Computers & Structures* 264 (2022) 106773, publisher: Elsevier.
- [54] U. Duh, G. Kosec, J. Slak, Fast variable density node generation on parametric surfaces with application to mesh-free methods, *SIAM Journal on Scientific Computing* 43 (2) (2021) A980–A1000.
- [55] H. Wendland, *Scattered data approximation*, Vol. 17, Cambridge university press, 2004.
- [56] M. Jančič, F. Strniša, G. Kosec, Implicit-explicit error indicator based on approximation order, in: 2022 7th International Conference on Smart and Sustainable Technologies (SpliTech), 2022, pp. 01–04. doi:10.23919/SpliTech55088.2022.9854342.
- [57] P. Daniel, A. Ern, I. Smears, M. Vohralík, An adaptive hp-refinement strategy with computable guaranteed bound on the error reduction factor, *Computers & Mathematics with Applications* 76 (5) (2018) 967–983.
- [58] G. Guennebaud, B. Jacob, et al., Eigen v3, <http://eigen.tuxfamily.org> (2010).
- [59] M. F. Wakeni, A. Aggarwal, L. Kaczmarczyk, A. T. McBride, I. Athanasiadis, C. J. Pearce, P. Steinmann, A p-adaptive, implicit-explicit mixed finite element method for diffusion-reaction problems, *International Journal for Numerical Methods in Engineering* (2022).
- [60] G. Kosec, J. Slak, M. Depolli, R. Trobec, K. Pereira, S. Tomar, T. Jacquemin, S. P. Bordas, M. A. Wahab, Weak and strong form meshless methods for linear elastic problem under fretting contact conditions, *Tribology International* 138 (2019) 392–402, publisher: Elsevier.
- [61] W. S. Slaughter, *The Linearized Theory of Elasticity*, Birkhäuser Boston, 2002, pages 351–352. doi:10.1007/978-1-4612-0093-2.